Energy & Environmental Science

ROYAL SOCIETY OF CHEMISTRY

PAPER

View Article Online
View Journal | View Issue

Cite this: *Energy Environ. Sci.*, 2024, **17**, 8810

Global softening to manipulate sound velocity for reliable high-performance MgAgSb thermoelectrics†

Airan Li, ‡[a] Longquan Wang,‡[ab] Jiankang Li[ab] and Takao Mori *[ab]

High-performance thermoelectric materials at room temperature are eagerly pursued due to their promising applications in the Internet of Things for sustainable power supply. Reducing sound velocity by softening chemical bonds is considered an effective approach to lowering thermal conductivity and enhancing thermoelectric performance. Here, different from softening chemical bonds at the atomic scale, we introduce a global softening strategy, which macroscopically softens the overall material to manipulate its sound velocity. This is demonstrated in MgAgSb, one of the most promising p-type thermoelectric materials at room temperature to replace $(Bi,Sb)_2Te_3$, that the addition of inherently soft organic compounds can easily lower its sound velocity, leading to an obvious reduction in lattice thermal conductivity. Despite a simultaneous reduction of the power factor, the overall thermoelectric quality factor B is enhanced, enabling softened MgAgSb by $C_{18}H_{36}O_2$ addition to achieve a figure of merit zT value of ~0.88 at 300 K and a peak zT value of ~1.30. Consequently, an impressive average zT of ~1.17 over a wide temperature range has been realized. Moreover, this high-performance MgAgSb is verified to be highly repeatable and stable. With this MgAgSb, a decent conversion efficiency of 8.6% for a single thermoelectric leg and ~7% for a two-pair module have been achieved under a temperature difference of ~276 K, indicating its great potential for low-grade heat harvesting. This work will not only advance MgAgSb for low-grade power generation, but also inspire the development of high-performance thermoelectrics with global softening in the future.

Received 7th August 2024,
Accepted 6th October 2024

DOI: 10.1039/d4ee03521f

rsc.li/ees

Broader context

Thermoelectrics can harvest waste heat from the environment to power numerous sensors in the Internet of Things, aiding the realization of a carbon-neutral society. Efficient thermal-electricity transfer requires thermoelectric materials to exhibit not only an excellent power factor but also an extremely low thermal conductivity. Traditionally, reducing sound velocity by softening chemical bonds at atomic scale is effective to decrease thermal conductivity and enhance thermoelectric performance, but this approach often involves trial and error to find suitable doping or alloying elements. In this work, we adopt a more macroscopic method by incorporating soft organic compounds, which could globally soften the materials and intentionally reduce sound velocity of material. We demonstrate that in MgAgSb, a promising p-type thermoelectric material with intrinsically low thermal conductivity at room temperature, adding soft organic compounds like fatty acid $C_{18}H_{36}O_2$ can effectively reduce its sound velocity, significantly lowering its lattice thermal conductivity further and improving its thermoelectric performance. Importantly, the addition of $C_{18}H_{36}O_2$ also enhances the reproducibility of high-performance MgAgSb. Based on this reliable MgAgSb, high conversion efficiency can be achieved, showcasing its potential for practical application in the Internet of Things in the future.

Introduction

Thermoelectric (TE) technology, which enables the mutual conversion of heat and electricity, holds great promise for power generation by harvesting waste heat.[1,2] With the rapid development of the Internet of Things (IoTs) recently, there arises a growing demand for high-performance TE materials near room temperature to sustainably power the numerous sensors.[3] However, the limited kinds of high-performance TE materials at room temperature hinder their widespread

[a] *Research Center for Materials Nanoarchitectonics (MANA), National Institute for Materials Science (NIMS), Namiki 1-1, Tsukuba, 305-0044, Japan. E-mail: MORI.Takao@nims.go.jp*
[b] *Graduate School of Pure and Applied Sciences, University of Tsukuba, Tennodai 1-1-1, Tsukuba, 305-8671, Japan*

† Electronic supplementary information (ESI) available. See DOI: https://doi.org/10.1039/d4ee03521f

‡ These authors contribute equally to this work.

application. Generally, the TE performance of a material is judged by the figure of merit, $zT = S^2\sigma T/\kappa$, where S is the Seebeck coefficient, σ is electrical conductivity, T is the absolute temperature and κ is thermal conductivity. According to this formula, outstanding TE materials necessitate not only a superior power factor PF = $S^2\sigma$ but also an ultralow κ.

In the past, various strategies have been employed to enhance zT by improving the PF.[4] These strategies include, but are not limited to, band engineering,[5,6] carrier scattering manipulation[7–9] and carrier concentration optimization,[10,11] which have led to the advancement of numerous high-performance TE materials since the last century.[12] Besides enhancing PF, decreasing κ is also a viable approach to boosting TE performance.[13–15] For most bulk materials, κ is composed of electronic thermal conductivity κ_e and lattice thermal conductivity κ_L, where κ_e depends on the transport of carriers (electrons and holes), and κ_L depends on the transport of phonons. According to the Wiedmann–Franz law, $\kappa_e = L\sigma T$ (L is the Lorenz number), κ_e has a strong positive relationship with σ. Therefore, κ_L is considered an independent TE parameter beyond S, σ and κ_e. Due to the complex relationship between S, σ and κ_e, the strategy targeting a decrease in κ_L is very attractive.

In bulk materials, κ_L is governed by the phonon transport and can be described by the "phonon gas" model, which gives rise to the formula = $1/3 \times c_v v_g^2 \tau$, where c_v, v_g, and τ represent specific heat, phonon group velocity, and phonon relaxation time, respectively. This suggests that decreasing κ_L or finding materials with inherently low κ_L requires materials to possess low c_v, v_g and τ. Typically, materials with liquid-like ions can exhibit a reduction of c_v,[16] and it is challenging to manipulate the c_v, because the energy carried by atoms approaches the Dulong–Petit limit of $3k_BT$ per atom in bulk materials at high temperatures. Therefore, decreasing v_g and/or τ become the main focus to obtain low κ_L material. Phonon relaxation time τ reflects the scattering process of phonons, including both intrinsic and extrinsic contributions. Intrinsic phonon scattering (Umklapp scattering, U) requires materials to possess large anharmonicity, which is an important characteristic of many high-performance TE materials, such as PbTe,[17] SnSe[18] and Mg_3Sb_2.[19,20] Besides intrinsic U scattering, extrinsic phonon scattering by point defects, dislocations, grain boundaries, nanoporous and nanoprecipitate has been frequently introduced into the material to decrease κ_L, leading to significant advancements in TE materials to achieve high zT values.[21–24]

It is worth noting that strengthening phonon scattering can also influence v_g.[25] Generally, phonons in materials can be categorized as acoustic phonons and optical phonons. Since the velocity of optical phonons approaches 0, the main contribution to v_g comes from acoustic phonons. Usually, the velocity of acoustic phonons can be approximated by the sound velocity v_s due to their equivalence in the long wavelength limit. At the microscopic atomic scale level, v_s is influenced by the chemical bonds.[26,27] Low force constants between atoms and large atomic mass are beneficial for achieving low v_s.[28] Doping to soften chemical bonds has been demonstrated to effectively decrease κ_L and enhance the performance of TE materials.[15] On the other hand, from a more macroscopic perspective, v_s is determined by the strength of the overall sound transport medium, meaning the softer the medium, the lower the v_s. This suggests that if the material can be globally softened, a decrease in κ_L can also be expected, which however, remains to be verified.

Traditionally, methods such as alloying, work hardening, grain refinement, and second-phase strengthening are commonly used to increase materials' strength. The rule of mixtures serves as a guideline when adding a second phase into the matrix to form composites, predicting the composite's strength by averaging the strengths of the matrix and second phase, weighted by their respective proportions.[29] Incorporating strong, hard second phases can significantly enhance materials' strength, as seen when adding strong SiC to Bi_2Te_3-based materials can improve their mechanical properties.[30,31] Conversely, adding a soft second phase can reduce overall material strength, potentially lowering v_s and leading to low κ_L and high zT. MgAgSb, regarded as one of the most promising p-type TE materials for replacing $(Bi,Sb)_2Te_3$ at room temperature, has garnered significant attention in the past.[32–34] Due to its high band degeneracy and inherently low κ_L, MgAgSb can achieve a zT value of $\sim$0.7 at room temperature and a peak zT value of $\sim$1.2.[35–39] Factors such as hierarchical weak chemical bonds, atomic disorder, local structural distortion and crystal-liquid duality have been identified as important contributors to its intrinsically low κ_L.[28,40–43] Recently, efforts to further lower κ_L have been realized by nanostructuring and introducing nanopores into MgAgSb, which strengthen phonon scattering and result in an enhanced zT value in the temperature range from 300 K to 473 K.[44] However, this ultrafine-grained and nanoporous MgAgSb faces the risk of grain growth at high temperatures, making it suitable for cooling applications at low temperatures rather than power generation at relatively high temperatures. Nevertheless, decreasing κ_L could be an effective way to improve the TE performance of MgAgSb.

In this work, we introduce and adopt a global softening strategy to decrease v_s of MgAgSb, aiming to reduce its κ_L and enhance its TE performance. Firstly, by adding inherently soft organic compounds, we demonstrate that the v_s of MgAgSb can be efficiently decreased. Then, focusing on the addition of $C_{18}H_{36}O_2$, we find that the v_s of MgAgSb can be gradually manipulated when adjusting the $C_{18}H_{36}O_2$ content. Despite a decreased PF, the overall TE quality factor B gets enhanced due to the much-decreased κ_L, resulting in a high zT of $\sim$0.88 at 300 K and a peak zT of $\sim$1.30. Further, we reveal that this high-performance MgAgSb is highly repeatable and stable as a result of $C_{18}H_{36}O_2$ addition. Finally, using this high-performance MgAgSb, we achieve a high conversion efficiency η of $\sim$8.6% and $\sim$7% for a single TE leg and a two-pair module, respectively, showing great potential for harvesting low-grade heat. This reliable high-performance MgAgSb paves the way for its practical usage for power generations in the future, and the proposed global softening strategy can also stimulate performance enhancement in other TE systems.

Results and discussions

Reduced sound velocity for high TE performance

Due to the close relationship between phonon group velocity and v_s, κ_L is closely related to v_s. As shown in Fig. 1a, the curve of v_s *versus* κ_L for most semiconductors reveals a positive proportion of κ_L to v_s,[28,45,46] indicating that materials with low v_s tend to possess low κ_L and have the potential to be high-performance TE materials. MgAgSb is one such material with an intrinsically low v_s of ~1921 m s^{-1} (or 1844 m s^{-1}), depending on the synthesis condition and composition.[28,36] This low v_s gives rise to the low κ_L of MgAgSb (~0.6 W m^{-1} K^{-1}). In this work, one-step ball milling has been used to synthesize MgAgSb, resulting in its v_s of 1826 m s^{-1} and κ_L of 0.58 W m^{-1} K^{-1}, similar to the literature.

As mentioned above, v_s is strongly dependent on sound transport medium. Therefore, globally softening the materials holds great promise for reducing v_s of material, consequently leading to a reduction in κ_L. Organic compounds, which are normally softer than inorganic compounds, are ideal as possible additives for the softening of overall materials. Zinc stearate ($C_{36}H_{70}ZnO_4$), magnesium stearate ($C_{36}H_{70}MgO_4$) and stearic acid ($C_{18}H_{36}O_2$), known for their universe usage in powder metallurgy,[62,63] have been chosen to be added to MgAgSb. As shown in Fig. 1b, the v_s of MgAgSb was successfully reduced from its original 1826 m s^{-1} to 1760 m s^{-1}, 1742 m s^{-1}, and 1731 m s^{-1} with $C_{36}H_{70}ZnO_4$, $C_{36}H_{70}MgO_4$ and $C_{18}H_{36}O_2$ addition, respectively. As a result, the reduced v_s leads to an obvious drop in κ_L of MgAgSb in the whole temperature range, as shown in Fig. 1c, where κ_L reaches 0.48 W m^{-1} K^{-1} at room temperature and 0.21 W m^{-1} K^{-1} at 573 K by $C_{18}H_{36}O_2$ addition, which further brings about the enhancement of zT in MgAgSb. As shown in Fig. 1d, MgAgSb by $C_{18}H_{36}O_2$ addition can achieve a high zT value of ~0.88 at 300 K and a peak zT value of ~1.30, which is excellent in the temperature range from 300 K to 573 K compared to the previous reports.[33,36,47–49] Moreover, this high zT is very competitive among state-of-art p-type TE materials (Fig. 1e).[50–58] With this high-performance MgAgSb, its single TE leg can achieve 3.6% and 8.6% maximum conversion efficiency under the temperature difference ΔT of about 80 K and 280 K, respectively, standing out as one of the best p-type single TE legs compared to PbSe, $AgSbTe_2$ and GeTe.[50,52,53,59–61]

Manipulating sound velocity by adjusting $C_{18}H_{36}O_2$ content

To delve deeper into the global softening strategy aimed at reducing v_s, varying amounts (0–1 wt%) of $C_{18}H_{36}O_2$ have been introduced into the matrix of MgAgSb. As shown in the X-ray diffraction (XRD) patterns in Fig. 2a, the addition of $C_{18}H_{36}O_2$ (0.25–0.75 wt%) does not alter the phase of MgAgSb, while when 1 wt% $C_{18}H_{36}O_2$ is added, a noticeable Sb secondary phase appears, which has been excluded from further discussion. Typically, $C_{18}H_{36}O_2$ is stable below 573 K but decomposes at around 633 K. The presence of $C_{18}H_{36}O_2$ in the MgAgSb can be evidenced by the increase in the vacuum of SPS chamber when the sintering temperature exceeds 700 K (Fig. S1, ESI†). Additionally, as shown in Fig. S2 (ESI†), the gradually increasing endothermic peak around 650 K in differential scanning

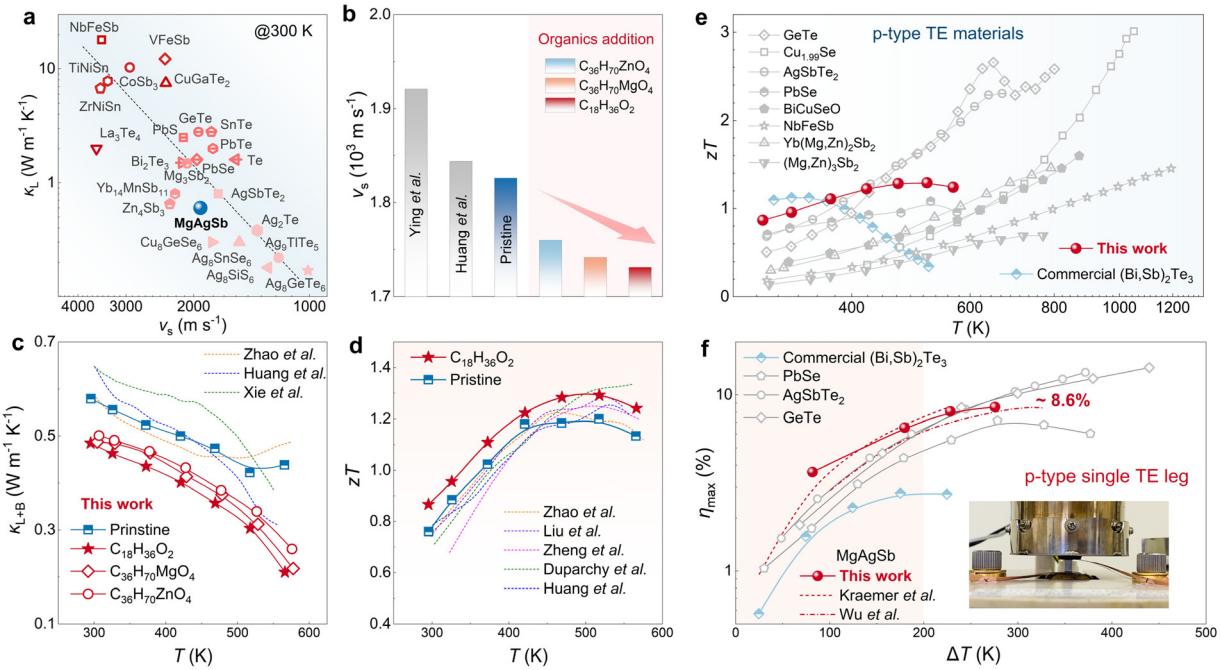

Fig. 1 Global softening for high-performance MgAgSb. (a) v_s *versus* κ_L at 300 K for various compounds;[28,45,46] (b) v_s of MgAgSb in literature[28,36] and this work; (c) T dependence of κ_L of MgAgSb without addition and with organic addition, and their comparison to literature;[33,36,44] (d) T dependence of zT of MgAgSb without addition and with $C_{18}H_{36}O_2$ addition, and their comparison to literature;[33,36,47–49] (e) T dependence of zT MgAgSb with $C_{18}H_{36}O_2$ addition and its comparison to other state-of-art p-type TE materials;[50–58] (f) applied ΔT dependence of maximum conversion efficiency η_{max} of MgAgSb single-leg and its comparison to other state-of-art p-type single-leg.[50,52,53,59–61]

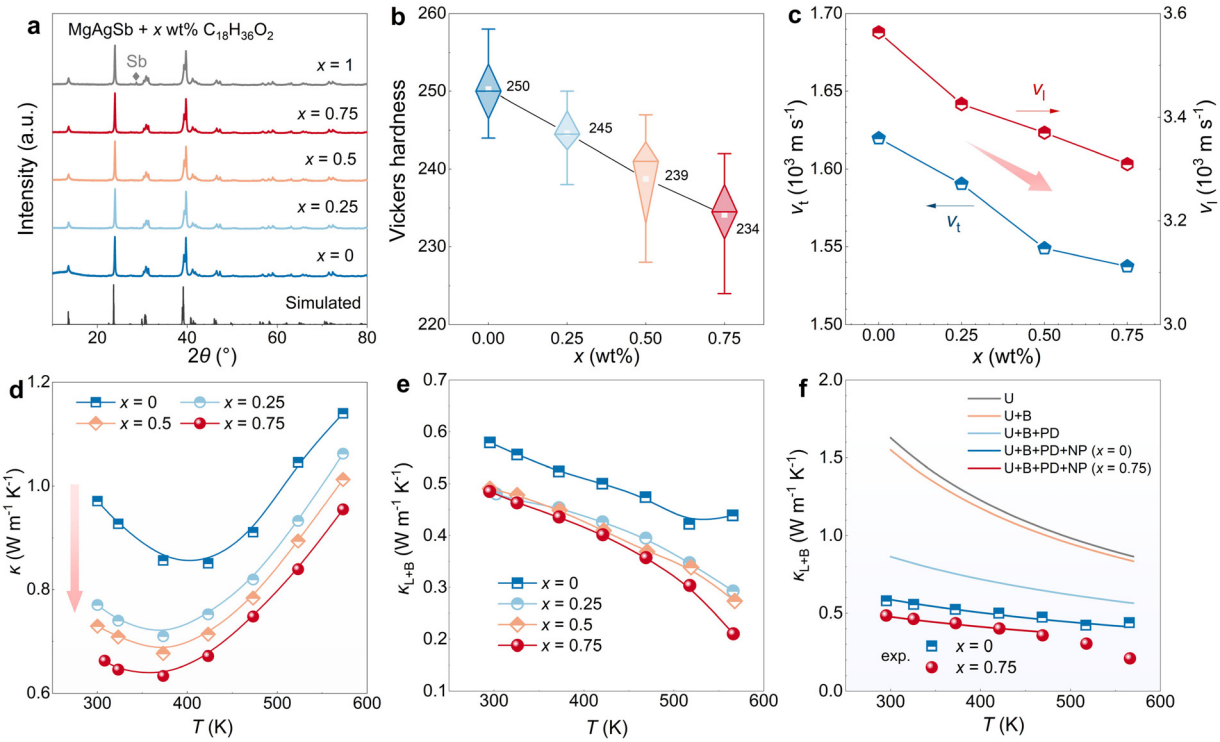

Fig. 2 $C_{18}H_{36}O_2$ addition to manipulate v_s and κ_L. (a) XRD patterns of MgAgSb with different $C_{18}H_{36}O_2$ addition (x = 0–1 wt%); (b) Vickers hardnesses, (c) v_l and v_t, T dependence of (d) κ and (e) κ_L of MgAgSb with x wt% $C_{18}H_{36}O_2$ addition (x = 0, 0.25, 0.5, 0.75); (f) experimental and simulated κ_L of MgAgSb with 0 wt% and 0.75 wt% $C_{18}H_{36}O_2$ addition.

calorimetry (DSC) curves of these $C_{18}H_{36}O_2$-added MgAgSb further confirms the successful addition of $C_{18}H_{36}O_2$ in MgAgSb.

Due to the addition of $C_{18}H_{36}O_2$, an expected softening effect on MgAgSb is observed, as indicated by the decreased Vickers hardness of MgAgSb shown in Fig. 2b. It should be noted that Vickers hardness is also influenced by changes in microstructure. Scanning electron microscopy (SEM) was used to observe the fracture morphology of pure MgAgSb and MgAgSb with 0.75 wt% $C_{18}H_{36}O_2$. As shown in Fig. S3 (ESI†), the grain size decreases in the sample with $C_{18}H_{36}O_2$ addition. However, despite the smaller grain size, the Vickers hardness of MgAgSb still decreases with $C_{18}H_{36}O_2$ addition. This is surprising, as according to the Hall–Petch relationship, smaller grain sizes usually result in increased strength or hardness. The decreased Vickers hardness suggests a more pronounced softening effect with $C_{18}H_{36}O_2$ addition.

The gradual softening of MgAgSb further leads to a corresponding gradual decrease in v_s. As displayed in Fig. 2c, both the longitudinal sound velocity v_l and transverse sound velocity v_t decrease with the increasing $C_{18}H_{36}O_2$ content. Consequently, the derived v_s of MgAgSb also gradually decreases. This suggests that v_s can be easily manipulated and tailored when adjusting the material's overall softness by different $C_{18}H_{36}O_2$ contents. Due to the deceased v_s, it correspondingly results in the decreased κ of MgAgSb. As shown in Fig. 2d, the κ of MgAgSb with 0.75 wt% $C_{18}H_{36}O_2$ addition decreases to 0.65 W m^{-1} K^{-1} at room temperature, nearly a 30% reduction compared to 0.95 W m^{-1} K^{-1} of MgAgSb without addition. Further, when subtracting κ_e, calculated based on the simplified single parabolic band (SPB) model (ESI† Note),[64] the decreased κ_L is also evident (Fig. 2e), where κ_L is decreased from 0.58 W m^{-1} K^{-1} to 0.48 W m^{-1} K^{-1} at room temperature.

It is important to note that the decreased v_s will also influence the scattering process of phonons. For example, both U scattering and nanoprecipitates (NP) scattering are inversely correlated with phonon group velocity, indicating that lower v_s will lead to more extensive phonon scattering. As shown in Fig. 2f, employing the Debye–Callaway model[65] and including the U scattering, boundary (B) scattering, point defect (PD) scattering and NP scattering[36,44,66] (Note and Table S1, ESI†), the simulated κ_L of MgAgSb without addition closely matches the experimental results. When incorporating the variation in v_s with 0.75 wt% $C_{18}H_{36}O_2$ addition, the simulated κ_L also aligns with the experiments around room temperature, confirming the significant role of v_s reduction in decreasing κ_L. Furthermore, it is worth noting that the minimum thermal conductivity κ_{min} is also related to v_s. The κ_{min} models proposed by Cahill *et al.*[67] Clarke *et al.*[68] or Snyder *et al.*[69] all exhibit a positive relationship with v_s. This suggests that materials with low v_s will also have a lower limit of thermal conductivity, offering more rooms and opportunities for further decreasing κ and achieving high TE performance.

Enhanced TE quality factor B and high average figure of merit

Generally, although κ_L is independent of other TE parameters (S, σ and κ_e), manipulating κ_L often affects electrical properties.

While $C_{18}H_{36}O_2$ addition could effectively lower κ_L of MgAgSb, it is also important that this addition has less detrimental impact on electrical performances to achieve high TE performance. As shown in Fig. 3a and b, it can be noticed that σ gradually decreases, whereas the S increases, which indicates a decrease in carrier concentration with increasing $C_{18}H_{36}O_2$ content. The overall PF decreases with higher $C_{18}H_{36}O_2$ content (Fig. 3c), indicating the deterioration of overall electrical transport performance. Intrinsically, based on the intrinsic electrical conductivity σ_0 (ESI† Note),[64] which evaluates the electrical transport performance potential, as well as weighted mobility μ_W[70] and electronic thermoelectric quality factor B_E,[71] it can be seen in Fig. S4 (ESI†) that σ_0, μ_W and B_E decrease with increasing $C_{18}H_{36}O_2$ content, confirm the intrinsic deterioration of electrical transport performance of MgAgSb with $C_{18}H_{36}O_2$ addition. Moreover, as shown in Fig. S5 (ESI†), the $T^{-1.5}$ relationship of μ_W in both pure MgAgSb and MgAgSb with $C_{18}H_{36}O_2$ indicates that carrier scattering is dominated by acoustic phonons. This suggests that the variation in S and σ is due to the addition of $C_{18}H_{36}O_2$ rather than the grain size reduction. Additionally, the calculated effective mass m^* for both pure MgAgSb and MgAgSb with $C_{18}H_{36}O_2$ addition is about 1.76 m_e, which matches well with the reported value,[44] suggesting that the band structure of MgAgSb remains unchanged with the addition of $C_{18}H_{36}O_2$.

However, the overall TE performance is not solely determined by electrical transport properties. Thermal transport properties also play a significant role. TE quality factor $B = S_0^2\sigma_0 T/\kappa_L$ is used to reflect the overall TE performance potential of the material, where S_0 is a constant and $2S_0 \approx 173$ μV K^{-1}. As shown in Fig. 3d, despite the decrease in σ_0, the decreased κ_L leads to an unchanged B factor at room temperature and even improved at high temperatures, suggesting the better TE potential for MgAgSb with $C_{18}H_{36}O_2$ addition. Due to the enhanced B factor at high temperature, it results in a superior zT of MgAgSb with 0.75 wt% $C_{18}H_{36}O_2$ addition, where zT value of 1.3 can be achieved at 523 K (Fig. 3e). Furthermore, despite the unchanged B factor at room temperature, the optimized S in MgAgSb with $C_{18}H_{36}O_2$ addition enables it to exhibit zT ~0.88 at 300 K. As a result, the zT_{avg} value reaches 1.17 in the temperature of 300–548 K, making it one of the best values compared to state-of-art MgAgSb, as shown in Fig. 3f.[33,36,47–49,72,73]

Highly reliable MgAgSb by repeatable synthesis and test

Besides the high TE performance, facile synthesis and excellent repeatability are additional benefits facilitated by the $C_{18}H_{36}O_2$ addition. Due to the complex phase transition of MgAgSb,[32] ball milling is usually preferred for synthesizing MgAgSb. However, powder adhesion to the jar walls during ball milling can pose a serious problem.[49] This not only makes it difficult to retrieve the powder but also leads to an inhomogeneous composition. The TE performance of MgAgSb is reported to be highly sensitive to its composition,[35,49] and powder adhesion is particularly problematic in its ball milling process.[49] Typically, a two-step ball milling method has been adopted to synthesize MgAgSb.[33,44] However, issues with repeatability of performance persist due to the uncontrollable powder adhesion during the synthesis of both the MgAg precursor and the final MgAgSb compounds.

$C_{18}H_{36}O_2$ is an effective process-control agent for addressing the problem of powder adhesion.[63] In this work, the addition of

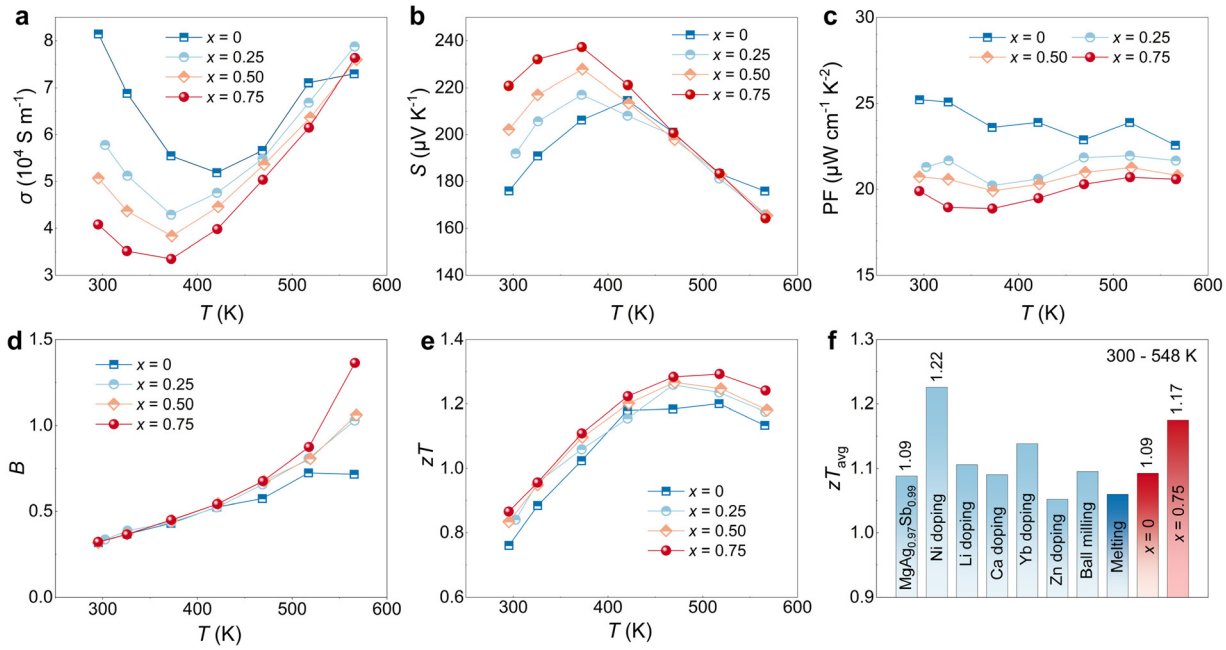

Fig. 3 Electrical properties of MgAgSb with $C_{18}H_{36}O_2$ addition. Temperature dependence of (a) σ, (b) S, (c) PF, (d) B factor, and (e) zT of MgAgSb with x wt% $C_{18}H_{36}O_2$ addition (x = 0, 0.25, 0.5, 0.75); (f) the average zT of MgAgSb in literature[33,36,47–49,72,73] and MgAgSb with no and 0.75 wt% $C_{18}H_{36}O_2$ addition.

$C_{18}H_{36}O_2$ not only softens MgAgSb globally but also resolves the powder adhesion issue. As shown in Fig. S6 (ESI†), compared to MgAgSb without $C_{18}H_{36}O_2$ addition, no power adhesives to the jar wall in MgAgSb with 0.75% $C_{18}H_{36}O_2$ addition, making it easy to retrieve the alloyed MgAgSb powder. It is worth noting that MgAgSb tends to contain various second phases even when undetected by XRD.[49] Energy-dispersive X-ray spectroscopy (EDS) mapping on both pure MgAgSb and MgAgSb with 0.75% $C_{18}H_{36}O_2$ addition has been used to identify distribution of constituent elements. As shown in Fig. S7 (ESI†), both samples display uniform element distributions, though some Sb-rich second phases are observable in pure MgAgSb. By addressing the powder adhesion issue with $C_{18}H_{36}O_2$, the second-phase problem can be alleviated. Another advantage of adding $C_{18}H_{36}O_2$ is that it enables a one-step ball milling process (5 hours) for synthesizing the material, making it much more time- and energy-efficient compared to the two-step process, which usually requires 5 hours followed by an additional 10 hours.[33,44] Importantly, due to the absence of powder adhesion, excellent repeatability of MgAgSb can be achieved. As shown in Fig. S8 (ESI†), three synthesized samples of MgAgSb from three separate ball milling jars exhibit very good phase purity. Furthermore, the TE transport properties of MgAgSb with $C_{18}H_{36}O_2$ addition are also repeatable. As shown in Fig. 4a–c, the data for S, σ and κ of three separate samples match well and are within 5% measurement error of S and σ, and 3% measurement error of κ, respectively.

In addition to the repeatable synthesis of MgAgSb conducted three times, the stability of TE properties in MgAgSb with $C_{18}H_{36}O_2$ addition warrants investigation, as $C_{18}H_{36}O_2$ may enter a liquid phase around its melting point of 343 K. Fig. S9 (ESI†) shows an endothermic peak in MgAgSb with 0.75 wt% $C_{18}H_{36}O_2$, likely due to its melting, but the peak is broad and weak because of its small content. Therefore, its impact on TE properties might be minimal. Further measurements of σ around 343 K show a smooth variation, indicating little influence from the potential melting of $C_{18}H_{36}O_2$ (Fig. S9, ESI†). Additionally, the stability of the sample under prolonged high-temperature exposure should also be explored. As shown in Fig. 4d–f, the electrical transport properties (S, σ, and PF) at 523 K and 573 K exhibit minimal changes over 30 measurements. The ratios of Seebeck coefficient (S/S_0), electrical conductivity (σ/σ_0), and power factor (PF/PF_0) for MgAgSb with 0.75 wt% $C_{18}H_{36}O_2$ remain at 1, indicating excellent stability even at elevated temperatures. Here, S_0, σ_0 and PF_0 represents the initial values of Seebeck coefficient, electrical conductivity and power factor, respectively. In all, as revealed above, despite being an organic compound, $C_{18}H_{36}O_2$ has quite good stability below 573 K, highlighting its significant role in achieving reliable high TE performance in MgAgSb.

High conversion efficiency of MgAgSb single-leg and two-pair modules

Due to the enhanced average TE performance over a wide temperature range, MgAgSb with 0.75 wt% $C_{18}H_{36}O_2$ addition is highly suitable for the low-grade heat harvesting. To access the materials' heat conversion ability, a single TE leg has been fabricated, which is sandwiched by two layers of MgCuSb due to its low contact resistance and stability.[74] As shown in Fig. 5a, it can be found that the contact resistance is very small, approximately 1 μΩ cm^2. For measuring η, various ΔT are

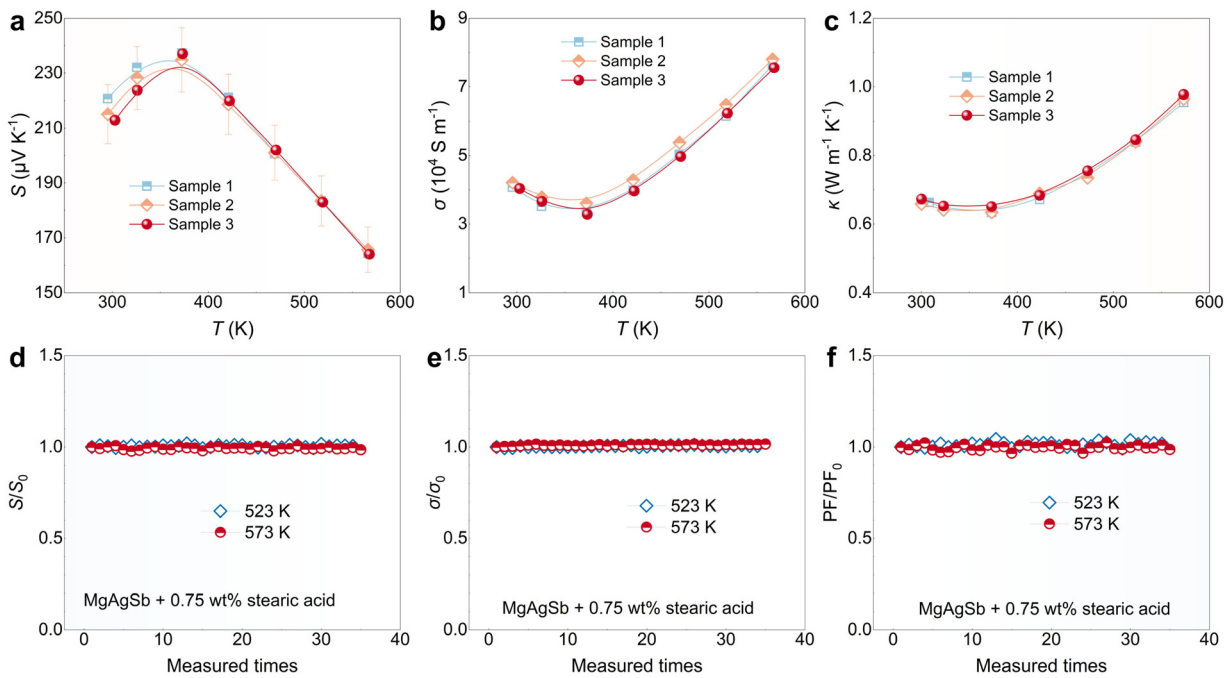

Fig. 4 Repeatable TE properties of MgAgSb with $C_{18}H_{36}O_2$ addition. T dependence of (a) σ, (b) S and (c) κ of MgAgSb with 0.75 wt% $C_{18}H_{36}O_2$ addition by three separate syntheses; (d) S/S_0, (e) σ/σ_0 and (f) PF/PF_0 of MgAgSb with 0.75 wt% $C_{18}H_{36}O_2$ acid addition under 523 K and 573 K for repeated measurements.

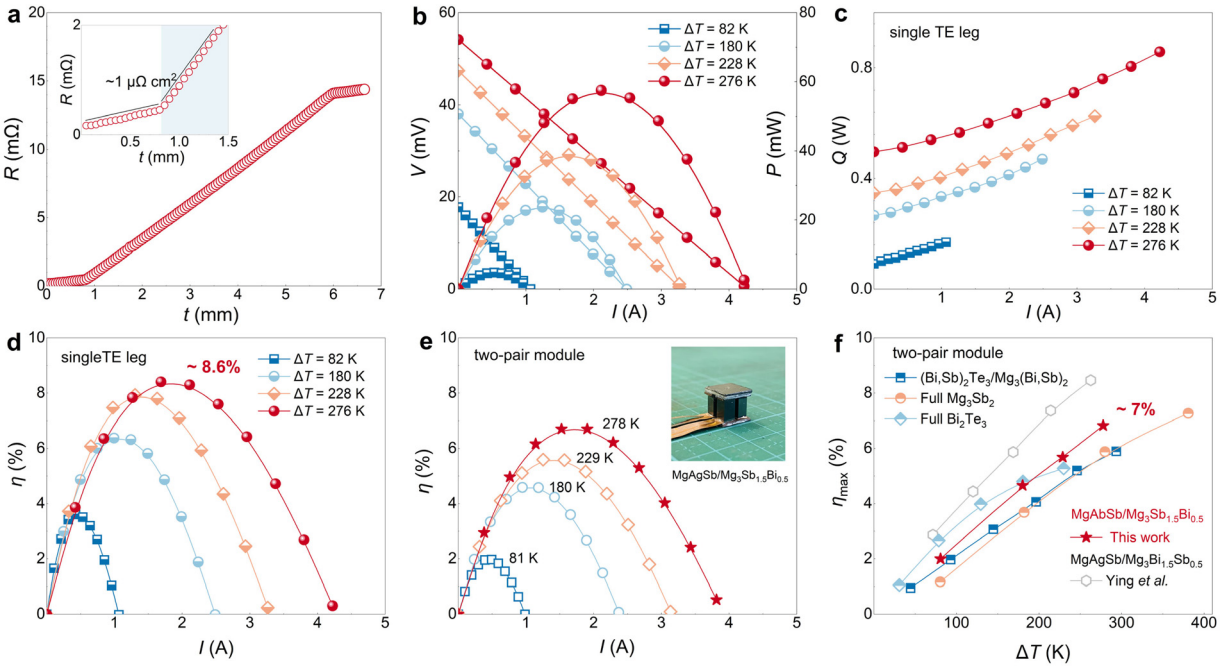

Fig. 5 Conversion efficiency of MgAgSb single TE leg and two-pair module. (a) Contact resistance between MgAgSb and MgCuSb in the single TE leg; (b) I dependence of V and P, and (c) Q of MgAgSb single TE leg under different ΔT; (d) I dependence of η of MgAgSb single TE leg, and (e) MgAgSb/$Mg_3Sb_{1.5}Bi_{0.5}$ two-pair module under different ΔT. The inset is the optical image of the two-pair module; (f) applied ΔT dependence of η_{max} of MgAgSb/$Mg_3Sb_{1.5}Bi_{0.5}$ and full Mg_3Sb_2-based, full Bi_2Te_3-based, $(Bi,Sb)_2Te_3/Mg_3(Bi,Sb)_2$-based and MgAgSb/$Mg_3Bi_{1.5}Sb_{0.5}$-based two-pair modules in literature.[76–79]

applied along the single TE leg.[75] The largest hot-side temperature T_h is limited to be 573 K considering the α-phase to β-phase transition of MgAgSb occurs in 573–583 K.[32] The measured output voltage V and output power P are displayed in Fig. 5b. The good linearity of the current-dependent V can be used to determine the internal resistance and open-circuit voltage of the single TE leg. A reduced slope indicates increased σ, which is consistent with the performance of our materials, and the increased open-circuit voltage is induced by the large ΔT. When T_h is 573 K (ΔT is ~276 K), the open-circuit voltage is 55 mV and the maximum output power P_{max} is 60 mW. The decreased κ of MgAgSb helps to efficiently utilize the heat energy by suppressing heat flow to the cold side Q (Fig. 5c), which consequently results in a high maximum conversion efficiency η_{max} of 3.6% under 82 K and 8.6% under 276 K (Fig. 5d). Furthermore, given the inherent stability of MgAgSb with $C_{18}H_{36}O_2$ as revealed above, it is anticipated that leg performance will remain stable when aging, if the interface performance does not degrade.

In addition to the single TE leg, a two-pair TE module has also been demonstrated, with its optical image shown in the inset of Fig. 5e. The n-type TE legs are based on Sb-rich $Mg_3Sb_{1.5}Bi_{0.5}$ due to its high chemical stability, as suggested by the recent study.[80] The TE performance of n-type $Mg_3Sb_{1.5}Bi_{0.5}$-based material is shown in Fig. S10 (ESI†), while Fig. S11 (ESI†) displays the measured V, P and Q under different applied ΔT and different applied current I. The T_h is also limited to 573 K, considering the phase transition of MgAgSb. As shown in Fig. 5e, η_{max} of this module can reach approximately 7% under ΔT of 278 K, comparable to recently reported Mg-based TE modules under ΔT of 300 K. It is noteworthy that this 7% conversion efficiency is based on n-type Sb-rich $Mg_3(Bi,Sb)_2$-based TE leg. Although its TE performance falls short of the Bi-rich $Mg_3(Bi,Sb)_2$-based material at room temperature,[38,59,74,76,81] it could exhibit much higher chemical stability, making it much more promising for practical applications.

Furthermore, the achieved η_{max} ~ 7% in MgAgSb/$Mg_3Sb_{1.5}Bi_{0.5}$-based module is quite impressive compared to full Mg_3Sb_2-based, full Bi_2Te_3-based and p-type $(Bi,Sb)_2Te_3$/n-type $Mg_3(Bi,Sb)_2$-based two-pair modules under the same ΔT.[77–79] This highlights the superior potential of p-type MgAgSb for low-grade waste heat harvesting. Moreover, repeatable η_{max} of both the single TE and the two-pair module have been achieved with two rounds of tests (Fig. S12, ESI†), demonstrating their good stability. If the TE performance of MgAgSb and Sb-rich $Mg_3Sb_{1.5}Bi_{0.5}$ is further improved, greater enhancement of η can be expected in the future.

Conclusions

In this work, we introduce a global softening strategy to decrease ν_s in TE materials, thereby enhancing their TE performance. Unlike traditional methods by softening chemical bonds at the atomic scale to reduce ν_s, our strategy stems from a macroscopic view, by introducing inherently soft organic compounds into the

material matrix to soften the overall material. Using MgAgSb, a promising p-type TE material, we demonstrate that adding various soft organics, such as zinc stearate ($C_{36}H_{70}ZnO_4$), magnesium stearate ($C_{36}H_{70}MgO_4$) and stearic acid ($C_{18}H_{36}O_2$), effectively reduce ν_s, which brings about the reduction of κ_L and enhancement of TE performance.

Specifically, it is found the ν_s of MgAgSb can be gradually tuned when adjusting $C_{18}H_{36}O_2$ contents, and an ultralow $\kappa_L \sim 0.48$ W m^{-1} K^{-1} can be achieved at room temperature in MgAgSb with 0.75 wt% $C_{18}H_{36}O_2$ due to the reduced ν_s and increased phonon scattering, greatly lower than the 0.58 W m^{-1} K^{-1} in MgAgSb without addition. Despite a simultaneous decrease in PF by $C_{18}H_{36}O_2$ addition, more reduction in κ_L results in an overall enhancement of the B factor. Consequently, a high zT value of $\sim$0.88 at 300 K and a peak zT value of $\sim$1.30 are achieved, which gives rise to an average zT of $\sim$1.17 in the temperature range of 300 K to 548 K, surpassing most state-of-art p-type TE materials. Moreover, the MgAgSb with $C_{18}H_{36}O_2$ shows good repeatability and high stability, indicating high reliability. Using this high-performance MgAgSb compound, we achieve a high η of $\sim$8.6% and $\sim$7% in a single TE leg and a two-pair module under ΔT of $\sim$276 K, respectively, demonstrating great potential for harvesting low-grade heat. This work not only advances high-performance MgAgSb for low-grade power generation but also proposes a global softening strategy to manipulate the ν_s for performance enhancement in thermoelectrics.

Methods

Materials synthesis

$MgAg_{0.97}Sb_{0.99}$ (denoted as MgAgSb in the main text and below) with x wt% $C_{18}H_{36}O_2$ (x = 0, 0.25, 0.5, 0.75, 1) were synthesized by using Mg turnings (99.95%), Ag powers (99.99%) Sb shots (99.999%), $C_{36}H_{70}ZnO_2$ power (99.9%), $C_{36}H_{70}MgO_2$ power (99.9%), and $C_{18}H_{36}O_2$ power (99.9%). The raw materials were weighted stoichiometrically and then put into the ball milling jar with the inside of argon. Then, the jaw was mechanically alloyed for continuously 5 h (SPEX-8000D). The alloyed samples were scratched from the jaw and then compressed into the bulk by vacuum spark plasma sintering (SPS-322Lx, Dr Sintering) in the carbon die of 10 mm diameter under 573 K and 60 MPa for 5 min. The relative density of all samples reaches $\sim$97%. $Mg_{3.2}In_{0.005}Sb_{1.5}Bi_{0.49}Te_{0.01}$ (denoted as $Mg_3Sb_{1.5}Bi_{0.5}$ in the main text and below) was prepared by using Mg turnings (99.95%), Te shots (99.999%), Bi shots (99.999%), Sb shot (99.999%), and In powder (99.99%), which was weighted stoichiometrically and loaded into the ball milling jar with inside of argon, and then ball milled for 5 h (SPEX-8000D). The obtained powder was consolidated by SPS (SPS-1080 System, SPS SYNTEX INC) under 973 K and 60 MPa for 20 min. MgCuSb was prepared by using Mg powder (99.95%), Cu powder (99.999%) and Sb powder (99.999%), which was weighted stoichiometrically and loaded into the ball milling jar with the inside of argon, and then ball milled for 20 h (5 cycles, each cycle contains 4 hours running and 30 minutes rest) (SPEX-8000D).

Characterization and measurements

The phases of obtained MgAgSb samples were characterized by using the X-ray diffractometer (SmartLab3, Rigaku) with Cu K_α radiation under 40 kV and 15 mA. The thermal analysis DSC was carried out by STA 449 (Netzsch) to check the existence of $C_{18}H_{36}O_2$, the samples were loaded into an Al crucible and heated to 773 K with a heating rate of 10 K min^{-1}. The fracture morphology of the sample were investigated by using scanning electron microscopy (FESEM, Hitachi SU8000), which is equipped with an energy dispersive spectrometer (EDS, XFlash FlatQUAD 5060 F) to study the samples' composition. The longitudinal (ν_l) and transverse (ν_t) sound velocity of obtained MgAgSb were measured by using a sing-around ultrasonic velocity measuring instrument (UVM-2, Ultrasonic Engineering Co., Ltd) with their sound velocity ν_s calculated according to $\nu_s^{-3} = (\nu_l^{-3} + 2\nu_t^{-3})/3$. The Vickers hardness of MgAgSb was measured by a micro-Vickers hardness tester (HMV-G, Shimadzu), where 10 different spots in one sample were measured. The zT of MgAgSb samples was calculated by the formula: $zT = S^2\sigma T/\kappa$, in which the S and the σ were measured by ZEM-3 (Advance Riko, $\pm$ 5% uncertainty) under helium atmosphere, and the κ was calculated by formula: $\kappa = D\rho C_p$, where the thermal diffusivity D was measured by LFA467 (Netzsch, $\pm$ 3% uncertainty), the sample density ρ was estimated by the Archimedes method, and heat capacity C_p was estimated by Dulong–Petit law. The Hall carrier concentration was measured by using a physical properties measuring systems, with an AC resistance option (PPMS, Quantum Design). The contact resistance of the MgAgSb/MgCuSb single TE leg was measured by a 2-axis resistance distribution measurement instrument (S1331, Mottainai energy).

Module fabrication and measurement

MgAgSb single TE leg was fabricated by sandwiching two layers of MgCuSb as the interface material and then sintered by SPS under 573 K and 60 MPa for 5 min. The obtained MgCuSb/MgAgSb/MgCuSb joints were cut into dice with dimensions of $\sim 3.8 \times 3.8 \times 6$ mm^3. The two-pair module was fabricated based on p-type MgCuSb/MgAgSb/MgCuSb TE legs and n-type 304 stainless steel/$Mg_3Sb_{1.5}Bi_{0.5}$/304 stainless steel TE legs. The output power and conversion efficiency of the single TE leg and two-pair module were measured by Mini-PEM, (ADVANCE RIKO, Japan) with cold-side temperature maintained at 293 K and hot-side temperatures ranging from 373 K to 573 K in a vacuum condition.

Author contributions

A. L., T. M. designed the project. A. L. prepared the samples and carried out the transport measurements and conversion efficiency measurement with the help of L. W. L. W. and J. L. provided the samples of $Mg_3(Sb,Bi)_2$ and MgCuSb, respectively.

A. L. analyzed the data and wrote the original manuscript. T. M. supervised the whole project. All the authors reviewed and edited the manuscript.

Data availability

All data generated or analyzed during this study are included in the published article and its ESI.† The data that support the findings of this study are available from the corresponding author upon request.

Conflicts of interest

T. M. and A. L. have filed one Japanese patent application (2024-111372) on the work described here. The remaining authors declare no competing interests.

Acknowledgements

This work was supported by JST Mirai Program (JPMJMI19A1).

References

1 J. He and T. M. Tritt, *Science*, 2017, **357**, eaak9997.
2 G. J. Snyder and E. S. Toberer, *Nat. Mater.*, 2008, **7**, 105–114.
3 I. Petsagkourakis, K. Tybrandt, X. Crispin, I. Ohkubo, N. Satoh and T. Mori, *Sci. Technol. Adv. Mater.*, 2018, **19**, 836–862.
4 T. Zhu, Y. Liu, C. Fu, J. P. Heremans, J. G. Snyder and X. Zhao, *Adv. Mater.*, 2017, **29**, 1605884.
5 Y. Pei, H. Wang and G. J. Snyder, *Adv. Mater.*, 2012, **24**, 6125–6135.
6 A. Li, C. Hu, B. He, M. Yao, C. Fu, Y. Wang, X. Zhao, C. Felser and T. Zhu, *Nat. Commun.*, 2021, **12**, 5408.
7 D. Liu, D. Wang, T. Hong, Z. Wang, Y. Wang, Y. Qin, L. Su, T. Yang, X. Gao, Z. Ge, B. Qin and L.-D. Zhao, *Science*, 2023, **380**, 841–846.
8 C. Hu, K. Xia, C. Fu, X. Zhao and T. Zhu, *Energy Environ. Sci.*, 2022, **15**, 1406–1422.
9 T. Mori, *Small*, 2017, **13**, 1702013.
10 Y. Pei, Z. M. Gibbs, A. Gloskovskii, B. Balke, W. G. Zeier and G. J. Snyder, *Adv. Energy Mater.*, 2014, **4**, 1400486.
11 M. Zhang, Z. Gao, Q. Lou, Q. Zhu, J. Wang, Z. Han, C. Fu and T. Zhu, *Adv. Funct. Mater.*, 2024, **34**, 2307864.
12 X.-L. Shi, J. Zou and Z.-G. Chen, *Chem. Rev.*, 2020, **120**, 7399–7515.
13 Z. Chen, X. Zhang and Y. Pei, *Adv. Mater.*, 2018, **30**, 1705617.
14 M. K. Jana and K. Biswas, *ACS Energy Lett.*, 2018, **3**, 1315–1324.
15 A. R. Muchtar, B. Srinivasan, S. L. Tonquesse, S. Singh, N. Soelami, B. Yuliarto, D. Berthebaud and T. Mori, *Adv. Energy Mater.*, 2021, **11**, 2101122.
16 H. Liu, X. Shi, F. Xu, L. Zhang, W. Zhang, L. Chen, Q. Li, C. Uher, T. Day and G. J. Snyder, *Nat. Mater.*, 2012, **11**, 422–425.
17 O. Delaire, J. Ma, K. Marty, A. F. May, M. A. McGuire, M. H. Du, D. J. Singh, A. Podlesnyak, G. Ehlers, M. D. Lumsden and B. C. Sales, *Nat. Mater.*, 2011, **10**, 614–619.
18 L.-D. Zhao, S.-H. Lo, Y. Zhang, H. Sun, G. Tan, C. Uher, C. Wolverton, V. P. Dravid and M. G. Kanatzidis, *Nature*, 2014, **508**, 373–377.
19 W. Peng, G. Petretto, G.-M. Rignanese, G. Hautier and A. Zevalkink, *Joule*, 2018, **2**, 1879–1893.
20 J. Ding, T. Lanigan-Atkins, M. Calderón-Cueva, A. Banerjee, D. L. Abernathy, A. Said, A. Zevalkink and O. Delaire, *Sci. Adv.*, 2021, **7**, eabg1449.
21 J. Xin, H. Wu, X. Liu, T. Zhu, G. Yu and X. Zhao, *Nano Energy*, 2017, **34**, 428–436.
22 A. U. Khan, K. Kobayashi, D.-M. Tang, Y. Yamauchi, K. Hasegawa, M. Mitome, Y. Xue, B. Jiang, K. Tsuchiya, D. Golberg, Y. Bando and T. Mori, *Nano Energy*, 2017, **31**, 152–159.
23 R. Deng, X. Su, Z. Zheng, W. Liu, Y. Yan, Q. Zhang, V. P. Dravid, C. Uher, M. G. Kanatzidis and X. Tang, *Sci. Adv.*, 2018, **4**, eaar5606.
24 R. He, T. Zhu, Y. Wang, U. Wolff, J.-C. Jaud, A. Sotnikov, P. Potapov, D. Wolf, P. Ying, M. Wood, Z. Liu, L. Feng, N. P. Rodriguez, G. J. Snyder, J. C. Grossman, K. Nielsch and G. Schierning, *Energy Environ. Sci.*, 2020, **13**, 5165–5176.
25 S. Han, S. Dai, J. Ma, Q. Ren, C. Hu, Z. Gao, M. Duc Le, D. Sheptyakov, P. Miao, S. Torii, T. Kamiyama, C. Felser, J. Yang, C. Fu and T. Zhu, *Nat. Phys.*, 2023, **19**, 1649–1657.
26 S. Lee, K. Esfarjani, T. Luo, J. Zhou, Z. Tian and G. Chen, *Nat. Commun.*, 2014, **5**, 3525.
27 J. He, Y. Xia, W. Lin, K. Pal, Y. Zhu, M. G. Kanatzidis and C. Wolverton, *Adv. Funct. Mater.*, 2022, **32**, 2108532.
28 P. Ying, X. Li, Y. Wang, J. Yang, C. Fu, W. Zhang, X. Zhao and T. Zhu, *Adv. Funct. Mater.*, 2017, **27**, 1604145.
29 H. S. Kim, *Mater. Sci. Eng., A*, 2000, **289**, 30–33.
30 J.-F. Li and J. Liu, *Phys. Status Solidi A*, 2006, **203**, 3768–3773.
31 L.-D. Zhao, B.-P. Zhang, J.-F. Li, M. Zhou, W.-S. Liu and J. Liu, *J. Alloys Compd.*, 2008, **455**, 259–264.
32 M. J. Kirkham, A. M. dos Santos, C. J. Rawn, E. Lara-Curzio, J. W. Sharp and A. J. Thompson, *Phys. Rev. B: Condens. Matter Mater. Phys.*, 2012, **85**, 144120.
33 H. Zhao, J. Sui, Z. Tang, Y. Lan, Q. Jie, D. Kraemer, K. McEnaney, A. Guloy, G. Chen and Z. Ren, *Nano Energy*, 2014, **7**, 97–103.
34 Z. Liu, J. Mao, J. Sui and Z. Ren, *Energy Environ. Sci.*, 2018, **11**, 23–44.
35 P. Ying, X. Liu, C. Fu, X. Yue, H. Xie, X. Zhao, W. Zhang and T. Zhu, *Chem. Mater.*, 2015, **27**, 909–913.
36 Y. Huang, J. Lei, H. Chen, Z. Zhou, H. Dong, S. Yang, H. Gao, T.-R. Wei, K. Zhao and X. Shi, *Acta Mater.*, 2023, **249**, 118847.
37 X. Tan, L. Wang, H. Shao, S. Yue, J. Xu, G. Liu, H. Jiang and J. Jiang, *Adv. Energy Mater.*, 2017, **7**, 1700076.
38 Z. Liu, W. Gao, H. Oshima, K. Nagase, C.-H. Lee and T. Mori, *Nat. Commun.*, 2022, **13**, 1120.
39 Z. Liu, N. Sato, W. Gao, K. Yubuta, N. Kawamoto, M. Mitome, K. Kurashima, Y. Owada, K. Nagase, C.-H. Lee, J. Yi, K. Tsuchiya and T. Mori, *Joule*, 2021, **5**, 1196–1208.

40 D. Li, H. Zhao, S. Li, B. Wei, J. Shuai, C. Shi, X. Xi, P. Sun, S. Meng, L. Gu, Z. Ren and X. Chen, *Adv. Funct. Mater.*, 2015, **25**, 6478–6488.
41 J. Li, X. Li, Y. Zhang, J. Zhu, E. Zhao, M. Kofu, K. Nakajima, M. Avdeev, P.-F. Liu, J. Sui, H. Zhao, F. Wang and J. Zhang, *Appl. Phys. Rev.*, 2024, **11**, 011406.
42 X. Li, P.-F. Liu, E. Zhao, Z. Zhang, T. Guidi, M. D. Le, M. Avdeev, K. Ikeda, T. Otomo, M. Kofu, K. Nakajima, J. Chen, L. He, Y. Ren, X.-L. Wang, B.-T. Wang, Z. Ren, H. Zhao and F. Wang, *Nat. Commun.*, 2020, **11**, 942.
43 J.-L. Mi, P.-J. Ying, M. Sist, H. Reardon, P. Zhang, T.-J. Zhu, X.-B. Zhao and B. B. Iversen, *Chem. Mater.*, 2017, **29**, 6378–6388.
44 L. Xie, J. Yang, Z. Liu, N. Qu, X. Dong, J. Zhu, W. Shi, H. Wu, G. Peng, F. Guo, Y. Zhang, W. Cai, H. Wu, H. Zhu, H. Zhao, Z. Liu and J. Sui, *Mater. Today*, 2023, **65**, 5–13.
45 W. Li, S. Lin, B. Ge, J. Yang, W. Zhang and Y. Pei, *Adv. Sci.*, 2016, **3**, 1600196.
46 M. Jin, S. Lin, W. Li, X. Zhang and Y. Pei, *Mater. Today Phys.*, 2021, **21**, 100508.
47 Z. Liu, Y. Wang, J. Mao, H. Geng, J. Shuai, Y. Wang, R. He, W. Cai, J. Sui and Z. Ren, *Adv. Energy Mater.*, 2016, **6**, 1502269.
48 Y. Zheng, C. Liu, L. Miao, C. Li, R. Huang, J. Gao, X. Wang, J. Chen, Y. Zhou and E. Nishibori, *Nano Energy*, 2019, **59**, 311–320.
49 A. Duparchy, L. Millerand, J. Camut, S. Tumminello, H. Kamila, R. Deshpande, A. Cowley, E. Mueller and J. de Boor, *J. Mater. Chem. A*, 2022, **10**, 21716–21726.
50 Z. Bu, X. Zhang, B. Shan, J. Tang, H. Liu, Z. Chen, S. Lin, W. Li and Y. Pei, *Sci. Adv.*, 2021, **7**, eabf2738.
51 H. Hu, Y. Ju, J. Yu, Z. Wang, J. Pei, H.-C. Thong, J.-W. Li, B. Cai, F. Liu, Z. Han, B. Su, H.-L. Zhuang, Y. Jiang, H. Li, Q. Li, H. Zhao, B.-P. Zhang, J. Zhu and J.-F. Li, *Nat. Mater.*, 2024, **23**, 527–534.
52 Y. Zhang, Z. Li, S. Singh, A. Nozariasbmarz, W. Li, A. Genç, Y. Xia, L. Zheng, S. H. Lee, S. K. Karan, G. K. Goyal, N. Liu, S. M. Mohan, Z. Mao, A. Cabot, C. Wolverton, B. Poudel and S. Priya, *Adv. Mater.*, 2023, **35**, 2208994.
53 S. Liu, Y. Wen, S. Bai, H. Shi, Y. Qin, B. Qin, D. Liu, Q. Cao, X. Gao, L. Su, C. Chang, X. Zhang and L.-D. Zhao, *Adv. Mater.*, 2024, 2401828.
54 Y. Gu, X.-L. Shi, L. Pan, W.-D. Liu, Q. Sun, X. Tang, L.-Z. Kou, Q.-F. Liu, Y.-F. Wang and Z.-G. Chen, *Adv. Funct. Mater.*, 2021, **31**, 2101289.
55 C. Fu, S. Bai, Y. Liu, Y. Tang, L. Chen, X. Zhao and T. Zhu, *Nat. Commun.*, 2015, **6**, 8144.
56 Z. Zhang, Y. Yan, X. Li, X. Wang, J. Li, C. Chen, F. Cao, J. Sui, X. Lin, X. Liu, G. Xie and Q. Zhang, *Adv. Energy Mater.*, 2020, **10**, 2001229.
57 Z. Ren, J. Shuai, J. Mao, Q. Zhu, S. Song, Y. Ni and S. Chen, *Acta Mater.*, 2018, **143**, 265–271.
58 K. Pang, L. Miao, Q. Zhang, Q. Pan, Y. Liu, H. Shi, J. Li, W. Zhou, Z. Zhang, Y. Zhang, G. Wu, X. Tan, J. G. Noudem, J. Wu, P. Sun, H. Hu, G.-Q. Liu and J. Jiang, *Adv. Funct. Mater.*, 2024, **34**, 2315591.
59 X. Wu, Y. Lin, C. Liu, Y. Wang, H. Li, B. Ge and W. Liu, *Energy Environ. Sci.*, 2024, **17**, 2879–2887.
60 D. Kraemer, J. Sui, K. McEnaney, H. Zhao, Q. Jie, Z. F. Ren and G. Chen, *Energy Environ. Sci.*, 2015, **8**, 1299–1308.
61 H.-L. Zhuang, H. Hu, J. Pei, B. Su, J.-W. Li, Y. Jiang, Z. Han and J.-F. Li, *Energy Environ. Sci.*, 2022, **15**, 2039–2048.
62 L. Lu and Y. F. Zhang, *J. Alloys Compd.*, 1999, **290**, 279–283.
63 L. Shaw, J. Villegas, H. Luo, M. Zawrah and D. Miracle, *Metall. Mater. Trans. A*, 2003, **34**, 159–170.
64 C. Hu, Z. Gao, M. Zhang, S. Han, C. Fu and T. Zhu, *Energy Environ. Sci.*, 2023, **16**, 5381–5394.
65 J. Callaway and H. C. von Baeyer, *Phys. Rev.*, 1960, **120**, 1149–1154.
66 W. Kim and A. Majumdar, *J. Appl. Phys.*, 2006, **99**, 084306.
67 D. G. Cahill, S. K. Watson and R. O. Pohl, *Phys. Rev. B: Condens. Matter Mater. Phys.*, 1992, **46**, 6131–6140.
68 D. R. Clarke, *Surf. Coat. Technol.*, 2003, **163–164**, 67–74.
69 M. T. Agne, R. Hanus and G. J. Snyder, *Energy Environ. Sci.*, 2018, **11**, 609–616.
70 G. J. Snyder, A. H. Snyder, M. Wood, R. Gurunathan, B. H. Snyder and C. Niu, *Adv. Mater.*, 2020, **32**, 2001537.
71 X. Zhang, Z. Bu, X. Shi, Z. Chen, S. Lin, B. Shan, M. Wood, A. H. Snyder, L. Chen, G. J. Snyder and Y. Pei, *Sci. Adv.*, 2020, **6**, eabc0726.
72 Z. Liu, Y. Wang, W. Gao, J. Mao, H. Geng, J. Shuai, W. Cai, J. Sui and Z. Ren, *Nano Energy*, 2017, **31**, 194–200.
73 Z. Liu, Y. Zhang, J. Mao, W. Gao, Y. Wang, J. Shuai, W. Cai, J. Sui and Z. Ren, *Acta Mater.*, 2017, **128**, 227–234.
74 L. Xie, L. Yin, Y. Yu, G. Peng, S. Song, P. Ying, S. Cai, Y. Sun, W. Shi, H. Wu, N. Qu, F. Guo, W. Cai, H. Wu, Q. Zhang, K. Nielsch, Z. Ren, Z. Liu and J. Sui, *Science*, 2023, **382**, 921–928.
75 R. Chetty, J. Babu and T. Mori, *Joule*, 2024, **8**, 556–562.
76 P. Ying, L. Wilkens, H. Reith, N. P. Rodriguez, X. Hong, Q. Lu, C. Hess, K. Nielsch and R. He, *Energy Environ. Sci.*, 2022, **15**, 2557–2566.
77 M. Jiang, Y. Fu, Q. Zhang, Z. Hu, A. Huang, S. Wang, L. Wang and W. Jiang, *Natl. Sci. Rev.*, 2023, **10**, nwad095.
78 L. Yin, F. Yang, X. Bao, W. Xue, Z. Du, X. Wang, J. Cheng, H. Ji, J. Sui, X. Liu, Y. Wang, F. Cao, J. Mao, M. Li, Z. Ren and Q. Zhang, *Nat. Energy*, 2023, **8**, 665–674.
79 X. Wu, Y. Lin, Z. Han, H. Li, C. Liu, Y. Wang, P. Zhang, K. Zhu, F. Jiang, J. Huang, H. Fan, F. Cheng, B. Ge and W. Liu, *Adv. Energy Mater.*, 2022, **12**, 2203039.
80 A. Li, P. Nan, Y. Wang, Z. Gao, S. Zhang, Z. Han, X. Zhao, B. Ge, C. Fu and T. Zhu, *Acta Mater.*, 2022, **239**, 118301.
81 P. Ying, R. He, J. Mao, Q. Zhang, H. Reith, J. Sui, Z. Ren, K. Nielsch and G. Schierning, *Nat. Commun.*, 2021, **12**, 1121.